Dynamics of the bcc→hcp transition in crystals under uniaxial stress

Hadrian Djohari,[1] Frederick Milstein,[2,*] and Dimitrios Maroudas[1,†]
[1]*Department of Chemical Engineering, University of Massachusetts, Amherst, Massachusetts 01003-3110, USA*
[2]*Departments of Mechanical Engineering and Materials, University of California, Santa Barbara, California 93106, USA*
(Received 15 January 2009; published 14 May 2009)

Molecular-dynamics simulations of a model alkali metal under ⟨100⟩ uniaxial load reveal a fundamental understanding of the atomistic kinematics and dynamics of the stress induced bcc→hcp lattice structural transition. The transformation itself is "Burgers-type," with opposing shearing of alternate {110} planes; however, shearing occurs on the {110} planes of zero shear stress. The results, including the singular nature of the lattice-parameter variations at the inception of the transition, are analyzed and explained within the framework of crystal elastic stability theory.

DOI: 10.1103/PhysRevB.79.174109 PACS number(s): 61.50.Ks, 64.70.K−, 81.30.Hd, 81.30.Kf

I. INTRODUCTION

Numerous metals, such as the alkali metals and iron, are known to undergo transformations among several crystalline structures including face-centered cubic (fcc), body-centered cubic (bcc), and hexagonal close-packed (hcp), depending on temperature and pressure.[1] The characteristics of bcc→hcp transitions, in general, have long been active topics of inquiry; see, e.g., Refs. 2–11 and the citations therein. In the generally accepted mechanism for the bcc→hcp transition, the $(1\bar{1}0)$ planes of the parent bcc crystal undergo shearing, in alternate [011] and $[0\bar{1}\bar{1}]$ directions, wherein the sheared $(1\bar{1}0)$ bcc planes become the (0001) planes of the new hcp crystal. This shearing mechanism for the bcc→hcp transformation, apparently first proposed by Burgers,[11] is based on analogous hexagonal geometry between the {110} planes in bcc crystals and the (0001) planes in hcp crystals.

In this paper, we present the results of isostress molecular-dynamics (MD) simulations of the Burgers bcc→hcp transition in a model alkali metal under a strict [100] uniaxial compressive load. Under this mode of loading, both intuition and classical plasticity theory imply that the specific {110} planes that undergo slip or shear during the transition should be the {110} planes on which the ⟨011⟩ shear stress τ is a maximum. Thus, it is worth noting that the specific family of {011} planes that undergo slip during the transformation instead consists of the {110} planes on which there exists no shear stress. Our MD simulations show that this counterintuitive behavior results directly from the existence of an invariant branching point[12] that lies on the [100] compressive loading path of bcc crystals,[13,14] and therefore, this behavior may be explained and understood simply from classical elastic stability and bifurcation theory, as put forth by Hill and Milstein.[12] Additionally, the dynamical mechanism for the inhomogeneous bcc→hcp transition observed in the present work is found to exhibit remarkable similarities to the shearing mechanism suggested by Milstein *et al.*,[13] for homogeneous bcc→fcc transitions in the alkali metals under [100] uniaxial loading, including the singular nature of the lattice-parameter variations at the inception of destabilization of the bcc phase.[13–15]

The paper is structured as follows. Section II outlines the principles of elastic stability analysis of cubic crystals under [100] uniaxial stress and the characteristics of bifurcation at the termini of stability ranges. A concise account of the interatomic potentials, MD simulation techniques, and methods of analysis of the simulation results is given in Sec. III. Our simulation results are presented in Sec. IV and are discussed in the context of the theoretical elastic stability and bifurcation analysis, as well as of previously published lattice-statics (LS) results. Finally, the main conclusions of our study are summarized in Sec. V.

II. THEORY

Homogeneous strains of a crystal lattice may be described by a set of "generalized coordinates" q_r $(r=1,\ldots,6)$ that specify the geometry of a deformed crystalline cell. Work-conjugate "generalized forces" p_r in a configuration q_r may be defined via the differential form

$$dE = p_r dq_r \tag{1}$$

(summation convention, $r=1,\ldots,6$), and "generalized moduli" c_{rs} via

$$dp_r = c_{rs} dq_s, \tag{2}$$

with

$$c_{rs} = \partial^2 E/(\partial q_r \partial q_s), \tag{3}$$

where E is the elastic strain energy per unit reference volume (e.g., per unit cell of the crystal). The incremental change in strain energy δE resulting from incremental changes in the cell's geometry δq_r is then

$$\delta E = p_r \delta q_r + (1/2) c_{rs} \delta q_r \delta q_s \tag{4}$$

to second order in the q_r. From a historical perspective, various choices of generalized coordinates q_r have been employed in the literature leading to diverse sets of generalized forces and elastic moduli. While this diversity is inconsequential in the absence of an applied load, for an elastically deformed crystal under generalized forces p_r, convexity of internal energy (i.e., the condition that $c_{rs}\ \delta q_r \delta q_s > 0$, for arbitrary δq_r when not all $\delta q_r = 0$, usually called the Born-stability criterion) is not coordinate invariant, in general.[12,14]

Consider the crystal to be in a current, elastically stable and homogeneously deformed state q_r under generalized

forces p_r and let the crystalline cell undergo any small arbitrary additional deformation of the chosen set q_r specified by the set δq_r. Elastic stability of the crystal then signifies that the combined incremental potential energy of the crystal and its external loading (i.e., the sum of the incremental elastic strain energy δE and external work δW) is positive for all possible arbitrary incremental variations δq_r. Therefore, the increment δW of external work must also be specified objectively to second order in the q_r, i.e.,

$$\delta W = p_r \delta q_r + (1/2) k_{rs} \delta q_r \delta q_s, \tag{5}$$

where the coefficients k_{rs} depend on the test configuration and the choice of variables q_r. The algebraic expression of the stability criterion, $\delta E - \delta W > 0$, then becomes

$$(c_{rs} - k_{rs}) \delta q_r \delta q_s > 0 \tag{6}$$

for arbitrary δq_r when not all $\delta q_r = 0$. The inequality (6) is, of course, coordinate invariant, and it reduces to the Born criterion in the absence of applied loads, i.e., when all $k_{rs}=0$.

Bifurcation of an initially stable crystal may occur on a primary path under a prescribed mode of loading at the "critical stage" where the quadratic form of relation (6) first passes from positive definite to semidefinite, i.e., at the instant at which the stability criterion (6) is first violated. At this stage, the homogeneous equations,

$$\delta p_r - k_{rs} \delta q_r = 0, \tag{7}$$

must have at least one eigensolution that causes the quadratic form to vanish; these equations are also necessarily coordinate invariant.[12]

Under [100] loading of an initially cubic crystal, $p_1 \neq 0$ in general, with all other $p_r=0$; the crystal becomes tetragonal on the primary path ($q_1 \neq q_2 = q_3$; cell edges remain perpendicular) with six independent moduli c_{rs}, viz. c_{11}, $c_{12}=c_{13}$, $c_{22}=c_{33}$, c_{23}, c_{44}, and $c_{55}=c_{66}$ (all other $c_{rs}=0$ and $c_{rs}=c_{sr}$). The differential relations [Eq. (2)] that govern an arbitrary differential disturbance, possibly taking the crystal from the primary tetragonal path, are then

$$dp_1 = c_{11} dq_1 + c_{12}(dq_2 + dq_3),$$

$$dp_2 = c_{12} dq_1 + c_{22} dq_2 + c_{23} dq_3,$$

and

$$dp_3 = c_{12} dq_1 + c_{23} dq_2 + c_{22} dq_3, \tag{8}$$

with

$$dp_4 = c_{44} dq_4, \quad dp_5 = c_{55} dq_5, \quad dp_6 = c_{55} dq_6. \tag{9}$$

For example, if the load was to remain uniaxial and coaxial with the [100] axis under the differential disturbance (i.e., p_1 and $dp_1 \neq 0$, in general, all other p_r and $dp_r=0$), the general solution to Eqs. (8) and (9) follows the primary tetragonal path ($dq_2=dq_3$) and gives the coordinate increments $(dq_1, \ldots, dq_6)$ on the primary tetragonal path as

$$\begin{aligned}(dq_1, dq_2, dq_3, dq_4, dq_5, dq_6) &= (c_{22} + c_{23}, -c_{12}, -c_{12}, 0, 0, 0) \\ &\times [c_{11}(c_{22} + c_{23}) - 2c_{12}^2]^{-1} dp_1.\end{aligned} \tag{10}$$

Of particular interest for studies of crystal instability and bifurcation under [100] loading are the two special cases wherein the crystalline cell may change its dimensions or shape differentially (i.e., not all $dq_r=0$) while the [100] generalized force p_1 remains constant and uniaxial (i.e., all $dp_r=0$, $p_1 \neq 0$, and all other $p_r=0$). One such case occurs when p_1 becomes stationary at an extremum on the primary path (i.e., where p_1 undergoes a local or global maximum or minimum on the primary path); from Eq. (10), this condition is seen to occur coincident with $c_{11}(c_{22}+c_{23})-2c_{12}^2=0$, although the precise location of this condition on the primary path depends on the specific designations of the p_r and c_{rs}, which in turn depend on the choice of generalized variables q_r. For example, if q_1 is the axial stretch λ_1 (i.e., the current length of a fiber coincident with the [100] axis divided by its length in the unstressed cubic state), p_1 varies as the uniaxial load F_1 in the [100] direction, and thus, it becomes stationary coincident with $dF_1=0$ at an extremum; by contrast, if the q_r are the Green strain variables, p_1 becomes stationary on the primary path at an extremum of the Green's conjugate stress, i.e., where $d(F_1/\lambda_1)=0$. As a consequence, in [100] tension, the maximum value in the Green conjugate stress is reached before the maximum load, while in compression, an extremum of the Green conjugate stress would be preceded by the load extremum. Thus, the location of an extremum of the generalized force is not coordinate invariant.

The second case of particular interest for an initially cubic crystal under [100] uniaxial load occurs at the "invariant $c_{22}=c_{23}$ eigenstate," i.e., substitution of $c_{22}=c_{23}$ into Eqs. (8) and (9) yields the secondary solution that admits branching under the conditions

$$dq_1 = 0, \quad dq_2 = -dq_3, \quad dq_4 = dq_5 = dq_6 = 0, \tag{11}$$

with

$$dp_r = 0 \ (r = 1, \ldots, 6). \tag{12}$$

Thus, the uniform eigendeformation at the branching point takes the crystal structure from the primary tetragonal path to a secondary orthorhombic branch [on which $q_1 \neq q_2 \neq q_3$, with the cell edges remaining orthogonal, according to Eq. (11)], and with the load remaining *dead* [according to Eq. (12)] during the differential eigendeformation. On the secondary path, at the branching point, the generalized Poisson ratios dq_2/dq_1 and dq_3/dq_1 are infinite and of opposite algebraic sign, while $dp_1/dq_1 = 0/0$ and, thus, it is indeterminate to first order. Since branching occurs under dead load, the second-order work terms in inequality (6) and in (7) vanish for this mode of bifurcation and, as a result, the location of the $c_{22}=c_{23}$ eigenstate on the primary tetragonal path is invariant (i.e., independent of the choice of geometric strain variables, in contrast with the location of the extrema of p_1 on the primary path). The invariance of the $c_{22}=c_{23}$ eigenstate simply requires q_1 and p_1 to be coaxial with the uniaxial load, which is, of course, coaxial with the unique axis of the tetragonal crystal, and q_2 and q_3 to be coaxial with the transverse tetragonal axes. A rigorous proof of this result is given by Hill and Milstein [Ref. 12, p. 3093].

In this paper, as a matter of notation, we employ "C_{rs}" to represent specifically the strain-dependent elastic moduli cal-

culated in our MD simulations, as outlined in Sec. III, and "c_{rs}" to represent the more general, or extensive, sets of elastic moduli of a crystal under load, defined by Eqs. (1)–(3). However, since the $c_{22}=c_{23}$ eigenstate is coordinate invariant, we may use the expressions "$c_{22}=c_{23}$ eigenstate" and "$C_{22}=C_{23}$ eigenstate" interchangeably. Similarly, the terminologies "C_{rs}" and "c_{rs}" are used interchangeably for an unstressed crystal.

Finally, we note that a tetragonal lattice may be described by either of the two distinct sets of orthogonal crystallographic axes, i.e., upon rotation of the "original" 2- and 3-axes by 45° about the 1-axis, a new set of axes are obtained on which the crystal maintains tetragonal symmetry. For example, if on the original, unrotated set of axes the crystalline cell is described as body-centered tetragonal, the tetragonal crystalline cell defined with respect to the rotated axes appears as face-centered tetragonal. As a result, the $c_{22}=c_{23}$ eigenstate, as defined with respect to the unrotated set of axes, occurs at the exact same point on the primary path as the "$c_{44}=0$" eigenstate, as defined with respect to the rotated axes and vice versa. Thus, it follows that the $c_{22}=c_{23}$ and $c_{44}=0$ eigenstates have the same quality of invariance, and the eigendeformation $\delta q_4 \neq 0$, all other $\delta q_r=0$, on one set of tetragonal axes is identical to $\delta q_2=-\delta q_3$, all other $\delta q_r=0$, on the other (rotated) set of tetragonal axes.

III. COMPUTATIONAL METHODS

In our study, interatomic interactions are modeled by a Morse potential that was parameterized[14] by fitting to the experimental values of the equilibrium lattice parameter and two elastic moduli (bulk modulus κ and shear modulus μ or, equivalently, C_{11} and C_{12}) of a bcc alkali metal (K). We employ a two-step computational procedure based on isothermal MD simulation. First, the initially bcc crystal's structural response and/or equilibrium geometric configuration is determined by isostress-isothermal MD simulation under constant uniaxial stress according to the isostress ansatz Lagrangian of Parrinello and Rahman.[16] Next, a canonical MD simulation is carried out, wherein the supercell shape and volume are held fixed at the state derived by the isostress MD simulation, in order to implement canonical strain fluctuation formulas[17] for calculation of the elastic moduli, C_{rs}. In the MD simulations, the equations of motion are integrated using a fifth-order Gear predictor-corrector algorithm with a time-step size of 10^{-14} s, which was sufficient to ensure the accuracy and numerical stability of the algorithm. The temperature is kept constant by rescaling the atomic velocities at every time step. Our computational results are well converged in terms of simulation parameters, such as the number of atoms in the MD supercell and the potential cutoff radius; for the results reported here, the number of atoms in the supercell ranged from 1024 to 3456 depending on loading conditions.

Further descriptions of our MD simulation methodology and implementation can be found in Refs. 4, 18, and 19, where similar potential functions have been used for MD assessments of theoretically derived elastic stability criteria and studies of the structural response of fcc crystals to

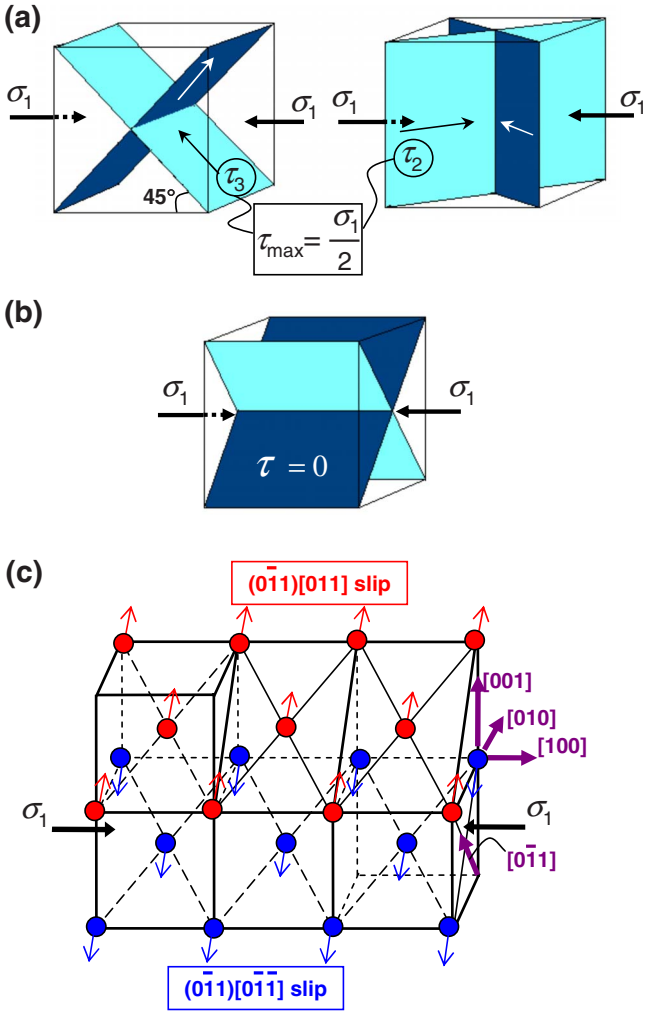

FIG. 1. (Color online) Illustrations of (a) the {110} planes of maximum shear stress, τ_{max}, under [100] uniaxial compression at a stress level σ_1, (b) the {110} planes of zero shear stress under the [100] uniaxial compression at stress σ_1, and (c) the mode of shearing (or slip) of adjacent $(0\bar{1}1)$ planes of zero shear stress, observed in the bcc crystals under [100] compression in the present study.

uniaxial loading,[18] as well as bcc (Ref. 4) and simple cubic[19] crystals to hydrostatic loading. Molecular-dynamics simulations, combined with elastic moduli computations, have also been used to study instabilities in other model crystals, e.g., fcc Au (Ref. 20) and SiC (Ref. 21) under hydrostatic stress.

IV. RESULTS AND DISCUSSION

Figure 1 shows the orientation of the {110} planes of a cubic crystal under [100] uniaxial compression at a stress level denoted by σ_1. The planes of maximum shear stress, τ_{max}, are illustrated in Fig. 1(a); these are the {110} planes that would be expected intuitively to undergo slip under this mode of loading. The {110} planes of zero shear stress are shown in Fig. 1(b). Counterintuitively, it is this family of zero-shear-stress planes that undergoes slip under the [100] uniaxial compression and facilitates the bcc→hcp transformation. The shearing mode observed in the MD simulations

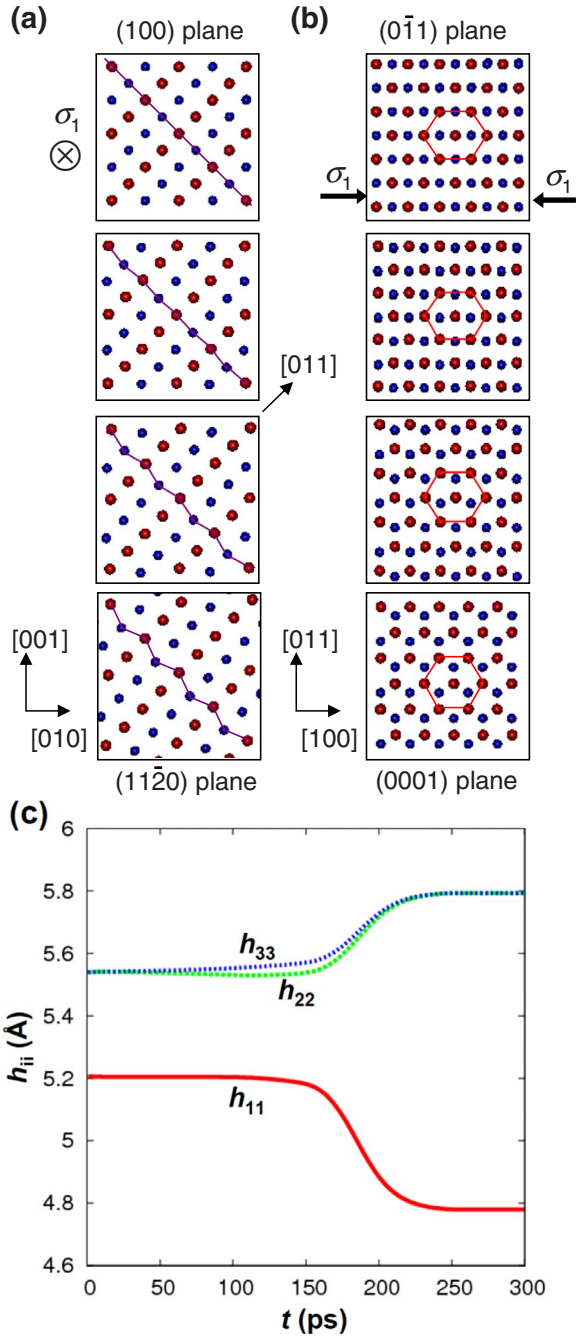

FIG. 2. (Color online) Planar views of a portion of the three-dimensional MD supercell showing the atomic configurations of (a) (100) planes and (b) (0$\bar{1}$1) planes during the bcc-to-hcp transformation as observed in our MD simulations at $\sigma_1=-61$ MPa and $T=1$ K; starting from the top, the shown snapshots correspond to times $t=0$, 139, 167, and 277 ps. The operating condition is just beyond the transformation onset, and atoms in adjacent (0$\bar{1}$1) planes are shaded (colored online) differently with the direction of the load as indicated. (c) Evolution of the diagonal elements of the transformation matrix $\mathbf{h}$ $(h_{ii}, i=1,2,3)$ during the same simulation.

is highlighted in Fig. 1(c), which shows consecutive (0$\bar{1}$1) planes undergoing slip in opposite ⟨011⟩ directions. The planar views of Figs. 2(a) and 2(b) show atomic configurations of the crystal before, during, and after the structural transformation, as observed in our MD simulations at $\sigma_1=-61$ MPa and $T=1$ K, which correspond to conditions just beyond the transformation onset. The (100) planes of the parent bcc crystal become the (11$\bar{2}$0) planes of the transformed hcp crystal, wherein the load remains uniaxial and normal to these planes; the (0$\bar{1}$1) planes in the bcc crystal become the (0001) planes of the hcp crystal. In the frames of Fig. 2(a), the direction of the load is perpendicular to the plane of the paper, while in the frames of Fig. 2(b) it is parallel to the plane of the paper and horizontal. Figure 2(c) shows the evolution of the supercell geometry before, during, and after destabilization of the initially bcc crystal resulting in a stable hcp crystal; the supercell shape is expressed by the 3×3 Parrinello-Rahman transformation matrix $\mathbf{h}\equiv[\mathbf{a},\mathbf{b},\mathbf{c}]$, where $\mathbf{a}$, $\mathbf{b}$, and $\mathbf{c}$ are the vectors that define the three edges of the supercell that intersect at the origin of the coordinate system.

Although the present MD simulations employ a relatively simple formulation for interatomic interactions (i.e., a Morse model of potassium), these simulations (i) yield a mechanical response that is in good *quantitative* agreement with prior LS calculations[13,22] based on more sophisticated quantum-mechanically formulated pseudopotential models (which are known to provide good descriptions of bonding in the alkali metals) and (ii) reveal *phenomenological* and *mechanistic* understanding of the dynamics of stress-induced bcc→hcp phase transformations. In particular, the quantum-mechanically-based LS calculations of the mechanical response of the alkali metals under uniaxial loadings revealed *homogeneous* branchings or bifurcations from primary [100] loading paths (of tetragonal symmetry) to secondary branch paths (of orthorhombic symmetry), leading to bcc→fcc and fcc→bcc phase transformations (under strict uniaxial load), wherein the resultant cubic phases were found to occur as "special" states on the orthorhombic paths. For initially bcc crystals, the bifurcations occurred in a state of [100] uniaxial compression, coincident with the invariant "$c_{22}=c_{23}$" eigenstate, as is discussed in Sec. II. At the branching point, to first order, the homogeneous eigendeformation was found to be in agreement with Eqs. (11) and (12), i.e., at the inception of bifurcation

$$d\lambda_1 = 0, \quad d\lambda_2 = -d\lambda_3 \neq 0, \tag{13}$$

under stationary load, i.e.,

$$dF_1 = dF_2 = dF_3 = 0, \tag{14}$$

where F_1 is the uniaxial load in the [100] direction, F_2 and F_3, respectively, are the loads (=0) in the [010] and [001] directions, and λ_i $(i=1,2,3)$ is the corresponding axial stretch (i.e., the corresponding lattice parameter in the current state, generally under load, divided by its value in a reference state). The singular nature of the homogeneous bifurcation is evident from the eigendeformation itself, i.e., the slopes

$$d\lambda_i/d\lambda_1 = \pm\infty (i=2,3) \tag{15}$$

and $dF_1/d\lambda_1=0/0$ (and hence is indeterminate to first order) at the branching point.

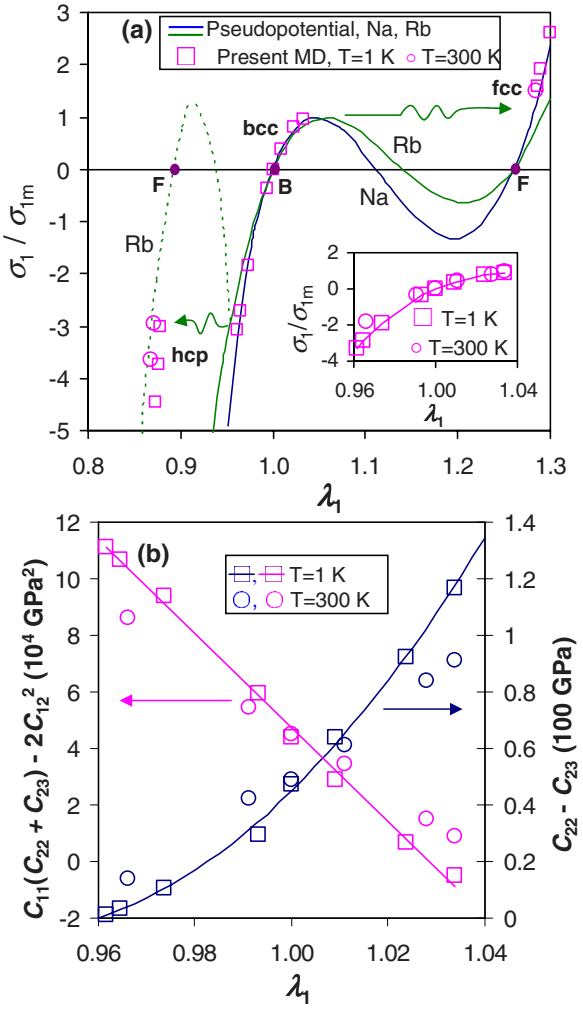

FIG. 3. (Color online) Mechanical response of model alkali metals to [100] uniaxial loading. (a) Normalized stress σ_1/σ_{1m} versus stretch λ_1; the solid lines represent the LS pseudopotential calculations of Rb (Ref. 13) and Na (Ref. 22) on the primary tetragonal path, while the broken line shows the secondary bco path that branches homogeneously from the primary path at the $C_{22}=C_{23}$ eigenstate, for the pseudopotential model of Rb (Ref. 13). B and F denote unstressed bcc and fcc structures, respectively. The arrows are used to indicate structural transformations observed in the MD simulations. The inset places emphasis on the MD results along the primary tetragonal path. (b) Results of present MD computations of elastic moduli combinations $C_{22}-C_{23}$ and $C_{11}(C_{22}+C_{23})-2C_{12}^2$ for the bcc crystal under uniaxial stress σ_1. In both (a) and (b), the open symbols denote the results of the MD simulations at $T=1$ K (squares) and 300 K (circles). The solid lines in (b) and in the inset to (a) represent least-squares fits to the MD results at $T=1$ K.

Figure 3(a) compares results of our MD simulations with the results of the pseudopotential LS computations of Refs. 13, 22, and 23. The pseudopotentials were formulated[24] specifically for the alkali metals, based on the Heine-Abarenkov local model potential and the Taylor approximation for electron correlation and exchange. With but *two* adjustable parameters, the model was shown to provide very good agreement with *nine* experimentally determined properties (i.e., the binding energies, atomic volumes, bulk moduli κ, shear moduli μ and μ', first-pressure derivatives of the three moduli, and second derivatives of κ with respect to pressure; the second derivatives of the shear moduli were also computed, but experimental data were lacking); excellent agreement between theoretical and experimental pressure-volume relations and relative phase stability among bcc and close-packed structures was also obtained.[24] In the pseudopotential LS computations ($T=0$), the considered eigendeformation at the $c_{22}=c_{23}$ eigenstate was uniform and homogeneous throughout the crystal (i.e., without shuffling of atomic planes in opposite directions).

As seen in Fig. 3(a), the results of our MD simulations for the stress-stretch relation on the primary tetragonal path follow close to the LS pseudopotential results of Refs. 13 and 22. The crystals are initially in the unstressed bcc configuration at λ_1 $(=\lambda_2=\lambda_3)=1$, state B in Fig. 3(a); under tension, the stress σ_1 undergoes a local maximum, σ_{1m}, within the range $1.04\leq\lambda_1\leq1.06$ (depending upon the metal and model) and under compression σ_1 reaches the invariant $C_{22}=C_{23}$ eigenstate within the range $0.95\leq\lambda_1\leq0.96$. On the primary tetragonal path, the crystal maintains body-centered (or equivalently, face-centered) tetragonal symmetry ($\lambda_1\neq\lambda_2=\lambda_3$, in general); this path, otherwise known as the tetragonal Bain transformation path of minimum energy barrier,[22] passes through the unstressed fcc configuration at the right-hand state F. Additionally, after transitioning (under compression) from the primary path to the uniaxially stressed hexagonal path,[25] the MD stress-stretch response follows reasonably close to the secondary body-centered orthorhombic (bco) branch path ($\lambda_1\neq\lambda_2\neq\lambda_3$) observed in Ref. 13 in the pseudopotential LS computations. This path contains the unstressed fcc structure at the left-hand state F; it is also equivalent to a primary [110] loading path of the initially unstressed fcc crystal, i.e., the unstressed fcc structure at the left-hand state F is oriented with its [110] axis aligned with the uniaxial load. The symmetry-breaking transformation from the body-centered tetragonal (bct) structure (on the primary path) to the uniaxially stressed hcp structure (on the secondary path), observed in the present MD simulations, is indicated by the "left-pointing" arrow in Fig. 3(a). Since the orthorhombic path is equivalent to the compressive response of the initially fcc crystal under [110] loading (see Fig. 1 in Ref. 13), the structural feature common to these two modes of loading is that the load is parallel to a close-packed plane [i.e., the (0001) plane of the hcp crystal and a {111} plane of the fcc crystal] and in a close-packed direction (i.e., the $[11\bar{2}0]$ direction of the hcp crystal and a ⟨110⟩ direction of the fcc crystal).

In tension, on the primary path, the initially bcc crystals reach σ_{1m} at $\sigma_1=46$ and 25 MPa for the LS pseudopotential models of Na and Rb, respectively, at the corresponding stretch values $\lambda_1=1.048$ and 1.057; for the "entire family" of the alkali metals, σ_{1m} ranged from 64.8 MPa for Li to 18.8 MPa for Cs, with corresponding values of λ_1 ranging from 1.041 to 1.059. In our MD simulations, under tension, both at 1 K and 300 K, the initially bcc crystal underwent a first-order nonsymmetry-breaking phase transformation indicated by the "right-pointing" arrow in Fig. 3(a) at $\lambda_1=1.034$ and $\sigma_1=20$ MPa; this corresponds to a tetragonal distortion that was found to take the crystal to the "fcc part" of the primary

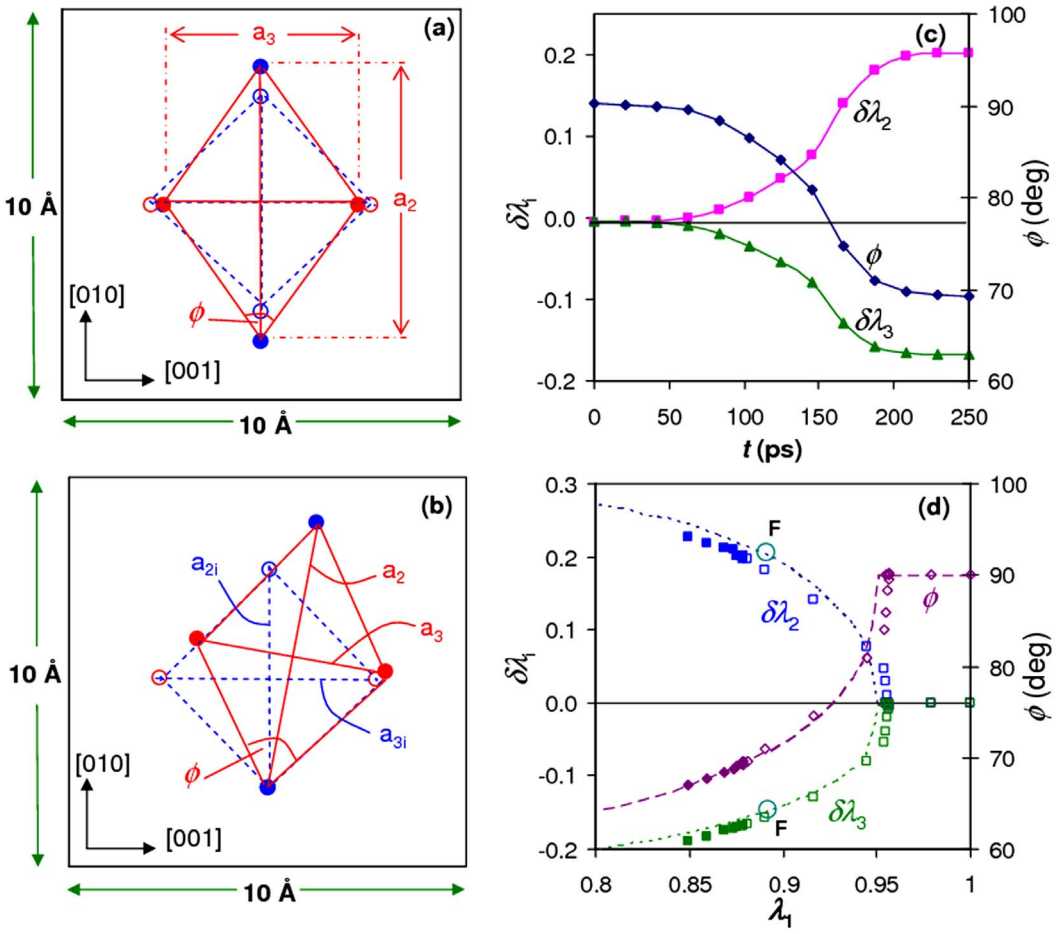

FIG. 4. (Color online) Relative movements of atoms in the (100) planes (a) in the course of bifurcation from the primary bct path to the secondary fco path (which takes the initial bcc crystal into the fcc configuration upon release of the stress after transformation) and (b) in the course of bifurcation from the primary bct path to the secondary hexagonal path (which takes the initial bcc crystal into the hcp configuration upon release of the stress after transformation). The transverse lattice parameters of the bct crystal, on the verge of destabilization, are $a_{2i}=a_{3i}$. Atoms in adjacent $(0\bar{1}1)$ planes are shaded (colored online) differently. (c) Evolution of the lattice parameters transverse to the load, $\delta\lambda_2=(a_2-a_{2i})/a_{2i}$ and $\delta\lambda_3=(a_3-a_{3i})/a_{3i}$, and shear angle, ϕ, in our MD simulations at $T=1$ K and $\sigma_1=-61$ MPa, during transition from the primary bct path to the secondary hexagonal path; similar behavior was observed at 300 K. (d) Variation in the transverse lattice parameters and shear angle, ϕ, with axial stretch, λ_1, for the transformations to the fcc structure (dashed lines, Ref. 13) and to the hcp structure (data points, present work). The solid and open symbols, respectively, represent equilibrium and transient MD results; the transient results are those varying with time in (c), while the equilibrium ones are for conditions $T=1$ K and $-310\leq\sigma_1\leq-61$ MPa.

tetragonal path in the present study. This transformation occurred in the neighborhood of a local incipient stress maximum and in the vicinity of the condition $C_{11}(C_{22}+C_{23})-2C_{12}^2=0$ as demonstrated in Fig. 3(b). This condition represents a "notional criterion" for elastic stability under load in that its inception depends upon the choice of strain variables, as is discussed in Sec. II; for metals, this condition typically occurs in the neighborhood of an extremum of the load and/or the stress. By contrast, as is discussed in Sec. II, the $C_{22}=C_{23}$ eigenstate is termed "invariant" in that its location on the primary [100] loading path is independent of the strain variables employed in the formulation of the elastic moduli (see Refs. 12 and 14 for a more thorough discussion of this topic).

Initially, for a stable bcc crystal, $C_{22}>C_{23}$ (i.e., $C_{11}>C_{12}$); under [100] compression, C_{22} decreases and C_{23} increases. In the present MD simulations, the $C_{22}=C_{23}$ eigenstate was found to occur at $\sigma_1/\sigma_{1m}=-3.05$ and -2.65 at $T=1$ and 300 K, respectively, at the corresponding values of stretch $\lambda_1=0.961$ and 0.953. For comparison, this state occurred at $\sigma_1/\sigma_{1m}=-3.02$ and -3.03, respectively, for the pseudopotential LS calculations for Na and Rb, with corresponding stretch values $\lambda_1=0.959$ and 0.952. For the entire family of the alkali metals, the $c_{22}=c_{23}$ eigenstate in the pseudopotential model was found in the range from $\sigma_1/\sigma_{1m}=-3.02$ (for Li) to -3.04 (for Cs) with corresponding values of $\lambda_1=0.962$ to 0.951. LS calculations based on the embedded-atom method (EAM) yielded similar eigenstates; i.e., for the four bcc alkali metals studied (Li, Na, K, and Rb), the values of σ_1/σ_{1m} at the invariant bifurcation point ranged from -2.78 to -3.28, with corresponding values of λ_1 ranging from 0.953 to 0.983.[26]

The crystal geometry associated with destabilization of the bcc structure at the $C_{22}=C_{23}$ eigenstate, under [100] load-

ing, is shown in Figs. 4(a)–4(d). Figures 4(a) and 4(b) compare the relative movements of atoms in the (100) plane of the parent bcc crystal before and after transformation (a) to the face-centered orthorhombic (fco) secondary branch[13] (which corresponds to an fcc crystal under [110] loading) and (b) to the secondary branch corresponding to the hcp structure under $[11\bar{2}0]$ load, as found in the present study. Figure 4(a) illustrates that the bifurcation leading to the fco path, described by Eqs. (11) and (13), can also be considered a shear deformation; similarly, the shear deformation observed in the present work can be described by local axial deformations, $\delta\lambda_2=(a_2-a_{2i})/a_{2i}$ and $\delta\lambda_3=(a_3-a_{3i})/a_{3i}$, where a_{2i} and a_{3i} are the lattice parameters of the initial bcc crystal aligned with [010] and [001] axes before destabilization and a_2 and a_3 are the corresponding lengths, in a current configuration, during and after transformation. The inceptions of both types of transformations are described by Eqs. (11) and (13) as seen in Fig. 4(d). Additionally, Fig. 4(d) shows the remarkable agreement between the geometric parameters during the two destabilization mechanisms; this is evident by the close agreement of the pseudopotential LS results for the bcc/bct→fcc/fco transformation with the present MD results for the bcc→hcp transformation. The mechanics (i.e., kinematics and dynamics) of the bcc→hcp transformations were similar at 1 and 300 K.

V. SUMMARY AND CONCLUSIONS

In summary, we carried out a theoretical study of the dynamics of the bcc→hcp structural transition in crystals under uniaxial stress based on MD simulations of the structural response of a model alkali metal to [100] uniaxial compressive loading. We found that the crystal undergoes a Burgers-type transformation with opposing shearing of alternate {110} planes that occurs on the {110} planes of zero shear stress. This interesting structural response is due to the existence of an invariant branching point on the [100] compressive deformation path of bcc crystals. In general, we have analyzed and understood the MD results on the basis of the classical theory of elastic stability and bifurcation in crystals under load. Particularly noteworthy are the similarities that we have found between the inhomogeneous bcc→hcp transformation analyzed in this study and the homogeneous bcc→fcc transition in alkali metals under [100] uniaxial loading; of special interest among them is the singular nature of the lattice-parameter variations at the inception of the transition from the bcc phase.

Finally, we note that the existence of the $c_{22}=c_{23}$ eigenstate in bcc crystals under [100] compression appears to be prevalent, which imbues the present work with fairly general implications. For example, in the EAM LS computations of Ref. 26, theoretical models of bcc Nb, Mo, and Fe that were formulated to reproduce identically empirical values of all second-order and third-order elastic moduli (i.e., the three C_{ij} and the six C_{ijk}) each exhibited $c_{22}=c_{23}$ eigenstates at values of $\lambda_1=0.747$, 0.756, and 0.904, respectively. For Nb and Mo, however, these eigenstates are reached at very small values of λ_1, which is consistent with the observation that neither of these metals undergo transformations from bcc to a close-packed structure,[1] whereas bcc Fe, with a "more accessible" $c_{22}=c_{23}$ eigenstate, is known to undergo a bcc→hcp transformation under shock loading.[2,3]

ACKNOWLEDGMENT

This work was supported in part by the National Science Foundation through Grants No. CTS-0205584 and No. CTS-0417770.

*Corresponding author. frdmlstn@engineering.ucsb.edu
†Corresponding author. maroudas@ecs.umass.edu

[1] D. A. Young, *Phase Diagrams of the Elements* (University of California Press, Berkeley, 1991).
[2] D. H. Kalantar *et al.*, Phys. Rev. Lett. **95**, 075502 (2005).
[3] K. Kadau, T. C. Germann, P. S. Lomdahl, and B. L. Holian, Science **296**, 1681 (2002).
[4] J. Zhao, D. Maroudas, and F. Milstein, Phys. Rev. B **62**, 13799 (2000).
[5] M. Ekman, B. Sadigh, K. Einarsdotter, and P. Blaha, Phys. Rev. B **58**, 5296 (1998).
[6] E. G. Moroni, G. Grimvall, and T. Jarlborg, Phys. Rev. Lett. **76**, 2758 (1996).
[7] R. M. Wentzcovitch, Phys. Rev. B **50**, 10358 (1994).
[8] V. P. Dmitriev, S. B. Rochal, Yu. M. Gufan, and P. Tole´dano, Phys. Rev. Lett. **62**, 2495 (1989); **60**, 1958 (1988); V. P. Dmitriev, Yu. M. Gufan, and P. Tole'dano, Phys. Rev. B **44**, 7248 (1991).
[9] R. S. Hixson, D. A. Boness, J. W. Shaner, and J. A. Moriarty, Phys. Rev. Lett. **62**, 637 (1989).
[10] F. Willaime and C. Massobrio, Phys. Rev. Lett. **63**, 2244 (1989).
[11] W. G. Burgers, Physica (Amsterdam) **1**, 561 (1934).
[12] R. Hill and F. Milstein, Phys. Rev. B **15**, 3087 (1977).
[13] F. Milstein, J. Marschall, and H. E. Fang, Phys. Rev. Lett. **74**, 2977 (1995).
[14] F. Milstein, in *Handbook of Materials Modeling*, edited by S. Yip (Springer, New York, 2005), pp. 1223-1279; F. Milstein, in *Mechanics of Solids*, edited by H. G. Hopkins and M. J. Sewell (Pergamon, Oxford, 1982), pp. 417–451.
[15] R. Hill, Math. Proc. Cambridge Philos. Soc. **92**, 167 (1982).
[16] M. Parrinello and A. Rahman, J. Appl. Phys. **52**, 7182 (1981).
[17] J. R. Ray, Comput. Phys. Rep. **8**, 109 (1988).
[18] F. Milstein, J. Zhao, and D. Maroudas, Phys. Rev. B **70**, 184102 (2004); F. Milstein, J. Zhao, S. Chantasiriwan, and D. Maroudas, Appl. Phys. Lett. **87**, 251919 (2005); H. Djohari, F. Milstein, and D. Maroudas, *ibid.* **89**, 181907 (2006).
[19] H. Djohari, F. Milstein, and D. Maroudas, Appl. Phys. Lett. **90**, 161910 (2007).
[20] J. Wang, J. Li, S. Yip, S. Phillpot, and D. Wolf, Phys. Rev. B **52**, 12627 (1995).
[21] M. Tang and S. Yip, Phys. Rev. Lett. **75**, 2738 (1995).
[22] F. Milstein, H. E. Fang, and J. Marschall, Philos. Mag. A **70**, 621 (1994).
[23] H. E. Fang, Ph.D. thesis, University of California, Santa Barbara,

1989.

[24] D. J. Rasky and F. Milstein, Phys. Rev. B **33**, 2765 (1986); F. Milstein and D. J. Rasky, *ibid.* **54**, 7016 (1996).

[25] For convenience, we refer to the secondary path, observed after branching, under load, in our MD simulations, as the "uniaxially stressed hexagonal path," or simply the "hexagonal path," although the space lattice is not strictly hexagonal when it is under the $[11\bar{2}0]$ load; after branching, and after the load is removed, the space lattice, of course, becomes hexagonal.

[26] F. Milstein and S. Chantasiriwan, Phys. Rev. B **58**, 6006 (1998).